CFD Predictions for Chemical Processing in a Confined Impinging-Jets Reactor

Ying Liu and R. O. Fox
Dept. of Chemical Engineering, Iowa State University, Ames, IA 50011

DOI 10.1002/aic.10633
Published online October 24, 2005 in Wiley InterScience (www.interscience.wiley.com).

Confined impinging-jets reactors (CIJR) offer many advantages for the chemical processing of rapid processes, such as precipitation and the production of organic nanoparticles. Nevertheless, due to the lack of predictive design criteria, the use of such a reactor for a new process currently requires a significant experimental campaign before it can be used commercially. Experimentally derived scale-up rules for CIJRs have recently been reported. Using carefully controlled experiments with a fast parallel-reaction system, the conversion of 2,2-dimethoxypropane (DMP) for a wide range of jet Reynolds numbers have been measured. The experimental conversion data can be accurately predicted using computational fluid dynamics (CFD) for the range of jet Reynolds number where the flow is turbulent. In addition, the CFD provides a wealth of detailed information on the reacting flow inside of the CIJR. Such information provides excellent guidance for improving the performance of the reactor by, for example, changes in the geometry. By clearly illustrating the ability of CFD to reproduce (without adjustable parameters) the experimental data for a CIJR, this study makes a significant step in the direction of "experiment-free" design and scale-up of chemical reactors. © 2005 American Institute of Chemical Engineers *AIChE J,* 52: 731–744, 2006
Keywords: DQMOM-IEM model, micromixing, turbulent reacting flow, confined impinging-jets reactor, computational fluids dynamics (CFD)

Introduction

A confined impinging-jets reactor (CIJR) consists of two high-velocity, coaxial liquid jets that collide and produce mixing times on the order of milliseconds. As discussed in detail elsewhere,[1] the use of confined impinging jets for chemical processing has been widely studied in the past. In recent years, there has been a renewed interest in these devices due to their ability to achieve very fast mixing relative to other fast processing steps. This fact has proven crucial in a number of high-value applications, such as the precipitation of biochemicals,[2,3] and the precise control of the particle-size distribution in the production of nanoparticles containing organic actives and block copolymer.[4,5]

Although CIJRs have been successfully used in production-scale processes,[1] scale-up rules have only recently been elucidated, based on a comprehensive experimental study. However, these scale-up rules require the user to run at least one experiment for any new geometry or operating conditions in order to fix a proportionality constant in the expression for the mixing time. In theory, by employing a computational approach, based on computational fluid dynamics (CFD) for turbulent reacting flow,[6] "experiment-free" design and scale-up of CIJRs should be possible. In practice, experiments would be required only to determine the fundamental rate constants appearing in the chemical kinetics. However, once determined, these constants could be used for arbitrary flow and geometrical conditions. Nevertheless, before such an approach can be used with confidence in industry, it must first be demonstrated that CFD predictions for a carefully designed and executed laboratory experiment are accurate and reliable.

Correspondence concerning this article should be addressed to Y. Liu at liuying@iastate.edu.

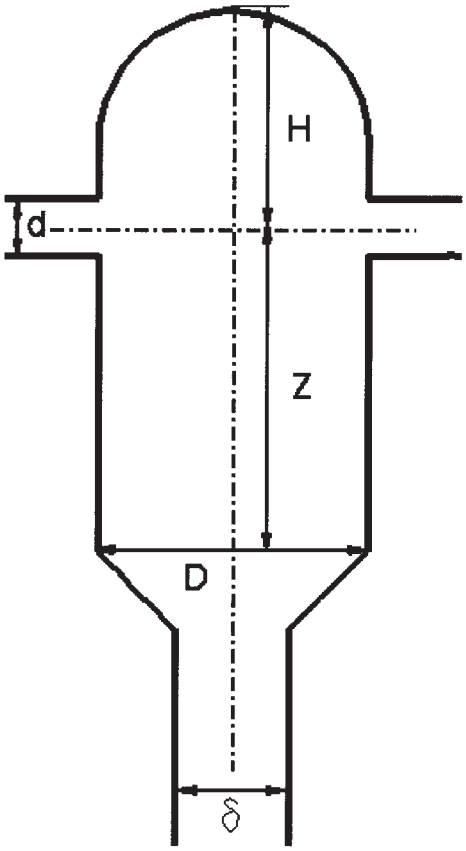

Figure 1. Confined impinging-jets reactor (CIJR).

The objective of this work is, thus, to validate a CFD model for mixing-sensitive reactions using the experimental data reported by Johnson and Prud'homme.[1] The CFD model is based on solving the composition probability density function (PDF) transport equation[6] using the direct-quadrature-method-of-moments (DQMOM).[7] The conditional molecular diffusion term is closed with the interaction-by-exchange-with-the-mean (IEM) model.[8] Wang and Fox[9] provide a complete description of the resulting DQMOM-IEM model. The geometry of the CIJR used in our CFD simulations is identical to the experiments, and is shown in Figure 1. The diameter of the impinging jets, d is 0.5 mm. Letting D, H, Z and δ represent the chamber diameter, height, length, and the outlet diameter, respectively, their scaled values are $D/d = 4.76$, $H = 0.8D$, $Z = 1.2D$, and $\delta = 2d$. More details on the CIJR and the experimental setup can be found in the original article.[1]

The remainder of this work is organized as follows: First, we review briefly the parallel-reaction system used in the experiments, and show that it can be modeled by two variables: mixture fraction and a reaction-progress variable. Following, we introduce the CFD model and discuss how it can be employed to study the different scales of mixing present in the CIJR. An overview of the simulation conditions is then followed by a detailed discussion of our results. We close by drawing conclusions from our study that are relevant to the use of CFD for analyzing the CIJR, and to chemical reactor scale-up in general.

Parallel-Reaction System

Reaction kinetics

In the experiments, a pair of second-order parallel reactions is employed to evaluate the extent of mixing.[10] The reaction stoichiometry can be expressed as

$$\mathrm{H^+}(A) + \mathrm{OH^-}(B) \xrightarrow{k_1} \mathrm{H_2O}(P_1)$$

$$\mathrm{H^+}(A) + \mathrm{CH_3C(OCH_3)_2CH_3}(D) + (\mathrm{H_2O}) \xrightarrow{k_2} \mathrm{H^+}(A) + \mathrm{CH_3COCH_3}(P_2) + 2\mathrm{CH_3OH}(P_3) \quad (1)$$

with rate constants $k_1 = 1.4 \times 10^8$ m^3/mol · s and

$$k_2 = 7.32 \times 10^7 \exp(-5556/T) 10^{(0.05434 + 7.07 \times 10^{-5} C_s)} \text{ m}^3/\text{mol} \cdot \text{s} \quad (2)$$

where C_s is the concentration of sodium chloride in the feed-streams. As shown in Eq. 1, hereinafter, we will refer to the reactants as, A, B, and C, and the products as P_1, P_2 and P_3. Note that the second reaction is catalytic so that A appears as both a reactant and a product with no net consumption. Non-premixed feed conditions are used with A in one stream, and B and D in the other stream. The reactor is operated in continuous mode with mass flow rate m_1 for the first stream containing A and $m_1 = m_2$ for the second stream containing B and D.

As discussed elsewhere,[1] since the first reaction is very rapid, when excess B is present the second reaction will take place only under conditions where mixing is slow compared to its reaction rate. Thus, the conversion of D is a sensitive measure of the extent of mixing in the CIJR. These authors[1] have, thus, varied the reaction rate (by changing the feed concentrations) and the mixing rate (by changing m_1) independently, and measured the conversion of D. Using CFD to model the reactor, in this work we will vary the same operating parameters and compare the predicted conversion to the experimental data.

Model variables

As discussed by Fox,[6] mixing between two inlet streams can be described by a mixture fraction ξ, which is not affected by chemistry. By convention, we will set $\xi = 0$ in the stream containing A and $\xi = 1$ in the other stream. Thus, the value of the average mixture fraction after complete mixing is

$$\bar{\xi} = \frac{m_2}{m_1 + m_2} = 0.5 \quad (3)$$

Any deviations from complete mixing will manifest themselves as values of the mixture fraction different than $\bar{\xi}$. Likewise,[6] the chemical kinetics in Eq. 1 can be described by two reaction-progress variables Y_1 and Y_2, which are zero in the feed streams, but otherwise always positive.

In terms of the mixture fraction and reaction-progress variables, the reactant concentrations are

$$c_A = A_0[1 - \xi - (1 - \xi_{s1})Y_1] \tag{4}$$

$$c_B = B_0(\xi - \xi_{s1}Y_1) \tag{5}$$

$$c_D = D_0(\xi - \xi_{s2}Y_2) \tag{6}$$

where

$$\xi_{s1} = \frac{A_0}{A_0 + B_0} \tag{7}$$

and

$$\xi_{s2} = \frac{A_0}{A_0 + D_0} \tag{8}$$

and A_0, B_0 and D_0 are the inlet molar concentrations of reactants *A, B*, and *D*, respectively. Thus, in the absence of chemical reactions (that is, $Y_1 = Y_2 = 0$), after complete mixing the reaction concentrations will depend only on $\xi = \bar{\xi}$.

By making the change of variables given in Eqs. 4 – 6, the reaction rates for the reaction-progress variables can be expressed as

$$S_1(\xi, Y_1) = \frac{k_1}{B_0\xi_{s1}} c_A c_B = B_0\xi_{s1}k_1\left(\frac{1 - \xi}{1 - \xi_{s1}} - Y_1\right)\left(\frac{\xi}{\xi_{s1}} - Y_1\right) \tag{9}$$

$$S_2(\xi, Y_1, Y_2) = \frac{k_2}{D_0\xi_{s2}} c_A c_D = B_0\xi_{s1}k_2\left(\frac{1 - \xi}{1 - \xi_{s1}} - Y_1\right)\left(\frac{\xi}{\xi_{s2}} - Y_2\right) \tag{10}$$

Note that since the reaction rates must always be nonnegative, the chemically accessible values of the reaction-progress variables will depend on the value of the mixture fraction. We will discuss this point further by looking next at limiting cases where the rate constant k_1 is very large and k_2 is finite.

Limiting cases

Due to the large value of k_1, the first reaction is essentially instantaneous compared to the characteristic mixing times in the CIJR. This implies that Y_1 can be written in terms of ξ by setting the corresponding reaction-rate expression (S_1) equal to zero

$$Y_{1\infty} = \min\left(\frac{\xi}{\xi_{s1}}, \frac{1 - \xi}{1 - \xi_{s1}}\right) \tag{11}$$

In order to avoid numerical difficulties associated with treating the first reaction with a finite-rate chemistry solver, we will use this infinite-rate approximation in our CFD simulations of the CIJR.

Note that Eq. 11 implies that *A* and *B* cannot coexist at any point in the flow. Using this infinite-rate approximation, we need only solve transport equations for ξ and Y_2, where the source term for Y_2, is now

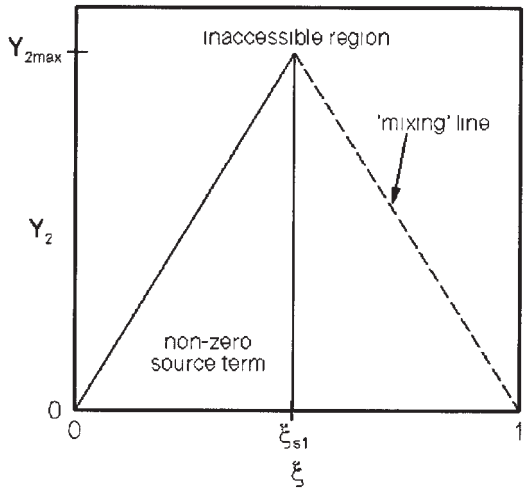

Figure 2. Region in $\xi - Y_2$ phase space with nonzero chemical source term, and the mixing line.

$$S_{2\infty}(\xi, Y_2) = B_0\xi_{s1}k_2\left(\frac{1 - \xi}{1 - \xi_{s1}} - Y_{1\infty}\right)\left(\frac{\xi}{\xi_{s2}} - Y_2\right) \tag{12}$$

Note that $S_{2\infty}$ must be non-negative, and, thus, the expression above only holds for ξ and Y_2 values that satisfy this condition. For all other values, $S_{2\infty}$ is null. Applying Eq. 11, we find that when $S_{2\infty}$ is nonzero, it equals

$$S_{2\infty}(\xi, Y_2) = A_0k_2\left(1 - \frac{\xi}{\xi_{s1}}\right)\left(\frac{\xi}{\xi_{s2}} - Y_2\right) \quad \text{if } 0 \le \xi \le \xi_{s1} \text{ and } 0 \le Y_2 \le \xi/\xi_{s2} \tag{13}$$

The region in $\xi - Y_2$ composition space where this chemical source term is non-zero is shown in Figure 2. Note that the maximum conversion of *D* occurs when $\xi = \xi_{s1}$ and corresponds to $Y_{2\max} = \xi_{s1}/\xi_{s2}$ or (using Eq. 6) to $c_D = 0$ (that is, complete conversion).

As mentioned earlier, the reactor is operated with excess *B* so that $\xi_{s1} = 0.4878$. Since equal flow rates are used for the inlet streams, the average mixture fraction is just outside the reaction region: $\xi_{s1} < \bar{\xi} = 0.5$. Thus, if mixing were much faster than the characteristic reaction time of Eq. 13 ($(A_0k_2)^{-1}$), the mixture fraction in all fluid particles would be equal to the mean ($\xi = \bar{\xi}$), and no reaction would occur so that $Y_2 = 0$.

In the opposite limit, the maximum attainable value for Y_2 when $\xi_{s1} \le \xi \le 1$ is the mixing line[6], defined by

$$Y_{2\text{mix}}(\xi) = Y_{2\max}\left(\frac{1 - \xi}{1 - \xi_{s1}}\right) \quad \text{for } \xi_{s1} \le \xi \le 1 \tag{14}$$

and shown as a dashed line in Figure 2. Using this expression, we find that the maximum attainable conversion is

$$X_{\max} = \frac{\xi_{s1}(1-\bar{\xi})}{\bar{\xi}(1-\xi_{s1})} \quad \text{for } \xi_{s1} \le \bar{\xi} \le 1 \tag{15}$$

In the experiments, the maximum conversion is, thus, $X_{\max} = 0.9524$, and would occur when the second reaction is very fast relative to mixing.

In summary, the accessible $\xi - Y_2$ phase space for this chemical system is given by the triangular region in Figure 2. Phase-space trajectories begin at the two feed streams [stream 1: (0,0) and stream 2: (1,0)] and end at the perfect-mixing point $(\bar{\xi}, \bar{Y}_2)$. If $\xi_{s1} < \bar{\xi}$, then the value of $\bar{Y}_2$ is determined by the amount of time spent in the region with nonzero source term (t_{mix}), and the characteristic time of the second reaction (t_r). If t_r is large compared to t_{mix}, then $\bar{Y}_2$ will be near zero. If the inverse is true, then $\bar{Y}_2$ will be near $Y_{2\max}$. The predicted value of $\bar{Y}_2$, thus, serves as a measure of the average mixing time for the CIJR.

Reactive Mixing Model

DQMOM-IEM model

In order to model reactive mixing using CFD, a micromixing model is needed to describe the interactions between chemistry and turbulent mixing.[6] In this work, we will use the two-environment DQMOM-IEM model.[9] The CFD model solves transport equations for the mixture fraction ξ_n, and reaction-progress variable Y_{2n} in the nth environment with $n = 1,2$. Each environment represents one inlet stream. The total number of transport equations needed to treat mixing and chemical reactions for the chemical system under consideration is five. The conserved scalars appearing in the model are p_1, $p_1\xi_1$, $p_2\xi_2$, p_1Y_{21} and p_2Y_{22}, where p_n is the mass fraction of the nth environment.

Denoting the mean fluid velocity and mean density as $\langle \mathbf{U} \rangle$ and ρ, respectively, the transport equation for the mass fraction of fluid coming from the first inlet (p_1) is

$$\frac{\partial \rho p_1}{\partial t} + \nabla \cdot \rho \langle \mathbf{U} \rangle p_1 = \nabla \cdot (\rho \Gamma_{\mathrm{T}} \nabla p_1) \tag{16}$$

and the mass fraction of fluid coming from the second inlet is $p_2 = 1 - p_1$. In Eq. 16, the turbulent diffusivity is defined as

$$\Gamma_{\mathrm{T}} = \frac{C_\mu}{Sc_{\mathrm{T}}} \frac{k^2}{\varepsilon} \tag{17}$$

with $C\mu = 0.09$ and $Sc_{\mathrm{T}} = 0.7$. k and ε are the turbulent kinetic energy, and the turbulent dissipation rate, respectively, and are computed using the $k - \varepsilon$ model. More details on turbulence modeling can be found elsewhere.[11]

The transport equations for the mixture fraction in the two environments are

$$\frac{\partial \rho p_1 \xi_1}{\partial t} + \nabla \cdot (\rho \langle \mathbf{U} \rangle p_1 \xi_1) = \nabla \cdot [\rho \Gamma_{\mathrm{T}} \nabla (p_1 \xi_1)] + \rho \gamma p_1 p_2 (\xi_2 - \xi_1) + \frac{\rho \Gamma_{\mathrm{T}}}{\xi_2 - \xi_1} (p_1 |\nabla \xi_1|^2 + p_2 |\nabla \xi_2|^2) \tag{18}$$

and

$$\frac{\partial \rho p_2 \xi_2}{\partial t} + \nabla \cdot (\rho \langle \mathbf{U} \rangle p_2 \xi_2) = \nabla \cdot [\rho \Gamma_{\mathrm{T}} \nabla (p_2 \xi_2)] + \rho \gamma p_1 p_2 (\xi_1 - \xi_2) + \frac{\rho \Gamma_{\mathrm{T}}}{\xi_2 - \xi_1} (p_1 |\nabla \xi_1|^2 + p_2 |\nabla \xi_2|^2) \tag{19}$$

The final two terms in these equations represent micromixing. If these terms are neglected, then it can easily be shown using Eq. 16 that ξ_1 and ξ_2 will be constant and equal to their inlet values. Thus, the effect of micromixing is to move the mixture fraction in each environment toward the local mean value, $\langle \xi \rangle$, or in other words to reduce the mixture-fraction variance $\langle \xi'^2 \rangle$.

The transport equations for the reaction-progress variable in the two environments are

$$\frac{\partial \rho p_1 Y_{21}}{\partial t} + \nabla \cdot (\rho \langle \mathbf{U} \rangle p_1 Y_{21}) = \nabla \cdot [\rho \Gamma_{\mathrm{T}} \nabla (p_1 Y_{21})] + \rho p_1 S_{2\infty}(\xi_1, Y_{21}) + \rho \gamma p_1 p_2 (Y_{22} - Y_{21}) + \frac{\rho \Gamma_{\mathrm{T}}}{Y_{21} - Y_{22}} (p_1 |\nabla Y_{21}|^2 + p_2 |\nabla Y_{22}|^2) \tag{20}$$

and

$$\frac{\partial \rho p_2 Y_{22}}{\partial t} + \nabla \cdot (\rho \langle \mathbf{U} \rangle p_2 Y_{22}) = \nabla \cdot [\rho \Gamma_{\mathrm{T}} \nabla (p_2 Y_{22})] + \rho p_2 S_{2\infty}(\xi_2, Y_{22}) + \rho \gamma p_1 p_2 (Y_{21} - Y_{22}) + \frac{\rho \Gamma_{\mathrm{T}}}{Y_{22} - Y_{21}} (p_1 |\nabla Y_{21}|^2 + p_2 |\nabla Y_{22}|^2) \tag{21}$$

Except for the chemical source term, these equations have the same form as those used for the mixture fractions. Note that the chemical source term ($S_{2\infty}$) is evaluated using the mixture fraction and reaction-progress variable in the particular environment. The average chemical source term $\langle S_{2\infty}(\xi, Y_2) \rangle$ will thus not be equal to $S_{2\infty}(\langle \xi \rangle, \langle Y_2 \rangle)$ unless micromixing occurs much faster than the second reaction.

Once the mixture fraction and the reaction-progress variable in each environment are known, the species concentrations in the nth environment can be obtained using Eqs. 4 – 6:

$$c_{An} = A_0[1 - \xi_n - (1 - \xi_{s1})Y_{1n}], \tag{22}$$

$$c_{Bn} = B_0(\xi_n - \xi_{s1}Y_{1n}), \tag{23}$$

$$c_{Dn} = D_0(\xi_n - \xi_{s2}Y_{2n}). \tag{24}$$

The mean concentrations are then defined by

$$\langle c_A \rangle = p_1 c_{A1} + p_2 c_{A2}, \tag{25}$$

$$\langle c_B \rangle = p_1 c_{B1} + p_2 c_{B2}, \tag{26}$$

$$\langle c_D \rangle = p_1 c_{D1} + p_2 c_{D2}. \tag{27}$$

The overall conversion of D, denoted by X, is computed using

$$X = 1 - \frac{\overline{\langle c_D \rangle}}{D_0 \bar{\xi}} \tag{28}$$

where the "mixing-cup" average of $\langle c_D \rangle$ at the outlet is defined by[12]

$$\overline{\langle c_D \rangle} = \frac{1}{m_3} \int_{\text{outlet}} \rho \langle c_D \rangle \langle \mathbf{U} \rangle \cdot \mathbf{n} dS \tag{29}$$

$m_3 = m_1 + m_2$ is the outlet mass flow rate, and $\mathbf{n}$ is the outward-directed normal vector on the outlet surface S. Note that $\overline{\langle c_D \rangle}$ would be equal to $\langle c_D \rangle$ if the outlet flow were completely macromixed. Also note that due to the small Reynolds number in the outlet tube, the outlet velocity is far from plug flow. Thus, the mixing-cup average in Eq. 29 cannot be replaced with the surface average when computing $\overline{\langle c_D \rangle}$.

Scales of mixing

In terms of the model variables, the mixture-fraction mean is defined by

$$\langle \xi \rangle = p_1 \xi_1 + p_2 \xi_2 \tag{30}$$

and the mixture-fraction variance by

$$\langle \xi'^2 \rangle = p_1 \xi_1^2 + p_2 \xi_2^2 - \langle \xi \rangle^2 \tag{31}$$

By summing Eqs. 18 and 19, the Reynolds-average transport equation for $\langle \xi \rangle$ is recovered

$$\frac{\partial \rho \langle \xi \rangle}{\partial t} + \nabla \cdot (\rho \langle \mathbf{U} \rangle \langle \xi \rangle) = \nabla \cdot (\rho \Gamma_T \nabla \langle \xi \rangle) \tag{32}$$

Using similar manipulations,[6] the Reynolds-average transport equation for $\langle \xi'^2 \rangle$ can also be recovered

$$\frac{\partial \rho \langle \xi'^2 \rangle}{\partial t} + \nabla \cdot (\rho \langle \mathbf{U} \rangle \langle \xi'^2 \rangle) = \nabla \cdot (\rho \Gamma_T \nabla \langle \xi'^2 \rangle) + 2\rho \Gamma_T |\nabla \langle \xi \rangle|^2 - 2\rho \gamma \langle \xi'^2 \rangle \tag{33}$$

The second term on the righthand side is a production term due to gradients in the mixture-fraction mean. The final term is a dissipation term due to micromixing.

Using the mixture-fraction mean and variance, we can define two types of segregation. The first type, large-scale segregation (LSS), is defined as deviations of $\langle \xi \rangle$ from the average $\bar{\xi}$ and can be measured by a LSS variance

$$\langle \xi'^2 \rangle_{\text{LSS}} = (\langle \xi \rangle - \bar{\xi})^2 \tag{34}$$

Starting from Eq. 32, the transport equation for the LSS variance can be found:

$$\frac{\partial \rho \langle \xi'^2 \rangle_{\text{LSS}}}{\partial t} + \nabla \cdot (\rho \langle \mathbf{U} \rangle \langle \xi'^2 \rangle_{\text{LSS}}) = \nabla \cdot (\rho \Gamma_T \nabla \langle \xi'^2 \rangle_{\text{LSS}}) - 2\rho \Gamma_T |\nabla \langle \xi \rangle|^2 \tag{35}$$

The characteristic decay time for LSS variance is, thus, given by

$$t_{\text{LSS}} = \frac{\langle \xi'^2 \rangle_{\text{LSS}}}{2\Gamma_T |\nabla \langle \xi \rangle|^2} \tag{36}$$

which in the mixing community is commonly called the "blend" or "macromixing" time (albeit defined in this case as a *local* quantity). Note that the LSS variance has no production term in its transport equation. Instead, $\langle \xi' \rangle_{\text{LSS}} = 0.25$ is nonzero in the inlet streams, and decays toward zero at the outlet. (Or at least it should if the residence time is long enough to allow for complete mixing).

The loss of LSS variance leads to production in Eq. 33 of small-scale segregation (SSS), which is measured by $\langle \xi'^2 \rangle$. The characteristic decay time for SSS variance is given by

$$t_{\text{SSS}} = \frac{1}{2\gamma} \tag{37}$$

and is commonly known in turbulent-mixing theory as the micromixing time.[6] In turbulent-transport models, the micromixing parameter γ is modeled by

$$\gamma = \frac{C_\phi}{2} \frac{\varepsilon}{k} \tag{38}$$

with $C_\phi \approx 2$ for high-Reynolds-number flow.[6] Note that if $C_\phi = 0$, the mixture fractions and reaction-progress variables in the DQMOM-IEM model will stay at their (constant) inlet values throughout the flow domain, and, hence, no reactions will occur in this limit. The SSS variance and the conversion of D are, thus, controlled directly by the model used for γ, and indirectly by t_{LSS} (since LSS variance must be eliminated before any reactions can occur).

For a fixed Schmidt number ($Sc = \nu/\Gamma$ where ν is the molecular kinematic viscosity and Γ is the molecular diffusivity), it is well known that C_ϕ is a function of the local turbulent Reynolds number.[13] In general, for $Sc \gg 1$ (that is, liquids), Eq. 38 with $C_\phi \approx 2$ overestimates the micromixing rate.[6] The *local* turbulence level can be quantified by a turbulent Reynolds number defined as [6]

$$Re_1 = \frac{k}{(\varepsilon \nu)^{1/2}} \tag{39}$$

where $\nu \approx 2.073 \times 10^{-6}$ in this work.

The dependence of C_ϕ on Re_1 can be understood by considering the shape of the scalar energy spectrum $E_\phi(\kappa)$ as a function of Re_1 for fixed $Sc = 1000$ (the shape is insensitive to Sc for values much larger than unity). Using a model scalar spectrum[6] for $Re_1 = (1, 10, 100, 1000)$, we find the spectra shown in Figures 3 and 4 where we have implicitly assumed

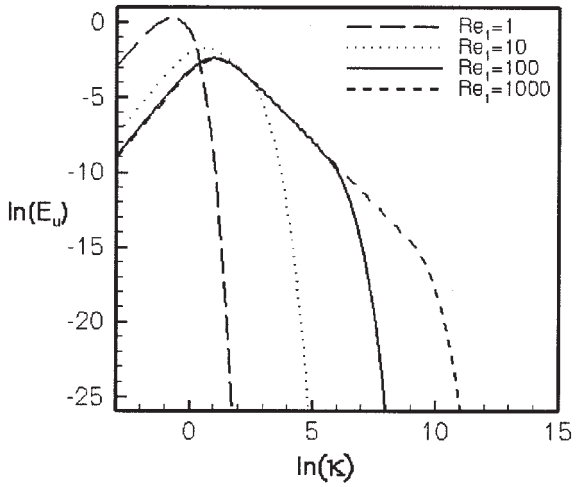

Figure 3. Dependence of model turbulent energy spectrum on the turbulent Reynolds number.

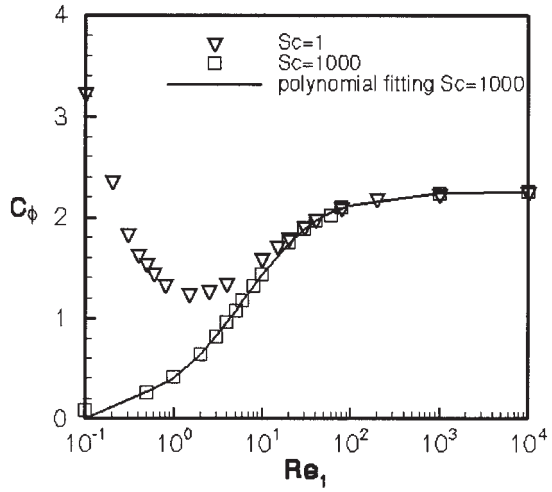

Figure 5. Dependence of C_ϕ on the turbulent Reynolds number for $Sc = 1$ (typical gases) and $Sc = 1000$ (typical liquids).

that the turbulence integral scale L_u is independent of Re_1 (that is, it is fixed by the geometry of the CIJR). Thus, the dimensionless wave number $\kappa = 1$ corresponds to the turbulence integral scale.[6] These scalar spectra can be interpreted as follows: For $Re_1 = 1$, the turbulence integral scale and the Kolmogorov scale η are equal so that the scalar energy spectrum has no inertial-convective subrange. Instead, for $1 < \kappa$, it is composed almost entirely of a viscous-convective subrange that scales like $E_\phi \sim \kappa^{-1}$, followed by an exponentially decaying viscous-diffusive subrange beginning near the Batchelor scale $\lambda_B = Sc^{-1/2}\eta$ (or, in terms of dimensionless wave numbers, near $\kappa = Sc^{1/2}Re_1^{3/2}$). At $Re_1 = 10$, there is still no well-defined inertial-convective subrange. However, at $Re_1 = 100$, a short inertial-convective subrange exists up to approximately $\kappa = Re_1^{3/2}$, which scales like $E_\phi \sim \kappa^{-5/3}$. This is followed by a viscous-convective subrange where $E_\phi \sim \kappa^{-1}$, and then by the viscous-diffusive subrange. Finally, at $\mathrm{Re}_1 = 1{,}000$ the scalar spectrum is fully developed with clearly visible inertial-convective, viscous-convective, and viscous-diffusive subranges. Likewise, in the model turbulent energy spectra (Figure 3), the $-5/3$ law can only be seen clearly at high-Reynolds numbers.

As explained by Fox[6] and originally proposed by Corrsin,[13] by integrating over the model scalar spectrum, we can compute the mechanical-to-scalar time-scale ratio R, which is equal to C_ϕ. Assuming Sc = 1,000, the dependence of C_ϕ on Re_1 found in this manner is shown in Figure 5. As expected, the shape of the scalar spectrum has a strong effect on C_ϕ, especially at low Reynolds numbers. In general, the decay rate of SSS variance is considerably smaller than the rate seen for a fully developed spectrum when $\mathrm{Re}_1 < 100$. The dependence of C_ϕ on Re_1 is approximated in our CFD simulations by the following expression

$$C_\phi = \sum_{n=0}^{6} a_n (\lg_{10} Re_1)^n \quad \text{for } Re_1 \geq 0.2 \tag{40}$$

which is also shown in Figure 5. Here $a_0 = 0.4093$, $a_1 = 0.6015$, $a_2 = 0.5851$, $a_3 = 0.09472$, $a_4 = -0.3903$, $a_5 = 0.1461$, and $a_6 = -0.01604$.

Because the local turbulent Reynolds number in the CIJR is found to be less than 65 for all of the flow conditions used in the experiments, accurate predictions of the chemical conversion are only possible by including low-Reynolds-number effects in the model for the micromixing rate. Finally, note that this procedure for finding the dependence of C_ϕ. on Re_1 can be used for other Schmidt numbers. For example, we have included in Figure 5 the results for $S_c = 1$, which would be appropriate for modeling gas-phase flows.

Differences in our interpretation of the micromixing time t_{SSS} as compared to "classical" micromixing theory[14,15] deserve comment. First, in the classical theory it is implicitly assumed that the flow is turbulent enough to allow for a clear separation of scales between the energy-containing and dissipation ranges. As seen in Figure 4, this will only occur if the local turbulence Reynolds number is greater than approximately 100. As men-

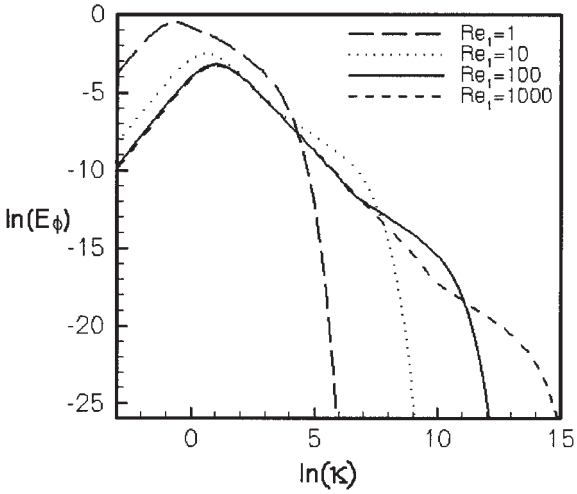

Figure 4. Dependence of scalar energy spectrum on the turbulent Reynolds number for $Sc = 1{,}000$.

Table 1. Average Inlet Concentrations for Various Values of the Characteristic Reaction Time

t_r (ms)	317	181	61	28	16.7	9.5	6.5	4.8
$A_0/2$ (mol/m^3)	4.69	8.21	24.36	53.06	88.96	156.39	228.56	309.50
$B_0/2$ (mol/m^3)	4.92	8.62	25.57	55.71	93.41	164.21	239.99	324.98
$D_0/2$ (mol/m^3)	4.69	8.21	24.36	53.06	88.96	156.39	228.56	309.50

tioned previously, even for the highest inlet jet Reynolds numbers investigated, the CIJR has Re_1 values that are much lower than 100. Thus, fully developed turbulence theory does not apply for the CIJR. Nevertheless, because of the lack of an inertial-convective subrange at low Reynolds numbers, t_{SSS} does not have pure inertial-range scaling either (that is, C_ϕ. is not constant). Instead, as the jet Reynolds number is increased, Re_1 increases leading to an increase in C_ϕ due to changes in the shape of the scalar spectrum. The fact that the experiments exhibit Kolmogorov scaling for the micromixing time[1] can be attributed to the presence of *only* the viscous-convective subrange for low Re_1. Thus, the question of how the micromixing time depends on the inlet jet Reynolds number is more complicated than the simple scaling theory presented by Johnson and Prud'homme.[1] We will return to this topic later when discussing the CFD simulation results.

Simulation Conditions

The CFD code Fluent 6.2 was used to solve the turbulence model and scalar transport equations. The computational grid consisted of at least 20880 hexahedral cells, with more cells required for grid-independent solutions at higher Reynolds numbers. The five dependent variables used in the DQMOM-IEM model are

$$X_1 = p_1, \quad X_2 = p_1\xi_1, \quad X_3 = p_2\xi_2, \quad X_4 = p_1Y_{21}, \text{ and } X_5 = p_2Y_{22},$$

where $p_2 = 1 - X_1$. These variables were implemented in Fluent 6.2 as user-defined scalars. The inlet conditions in the first inlet stream are $X_1 = 1$ and $X_2 = X_3 = X_4 = X_5 = 0$, and in the second inlet stream $X_1 = X_2 = 0$, $X_3 = 1$, and $X_4 = X_5 = 0$. Note that by definition, $\xi_1 = 0$ and $\xi_2 = 1$ in both inlet streams. Thus, for example, whenever $p_2 = 0$ the ratio $X_3/p_2 = 1$. The flow rates of the two inlet streams are equal. Therefore, under perfectly mixed conditions, the outlet values for the mass fractions would be $p_1 = p_2 = 0.5$. The properties of the flow are assumed to be constant. The density and the viscosity are 962.5 kg/m^3 and 0.001995 kg/m · s, respectively.

The characteristic reaction time is defined as $t_r = (k_2C_{A0})^{-1}$, where C_{A0} is the average concentration of A after mixing as if no reaction had occurred

$$C_{A0} = (1 - \bar{\xi})A_0 = 0.5A_0. \tag{41}$$

The temperature is assumed to be 298 K and kept constant. Therefore, the rate constant (Eq. 2) based on the inlet stream containing A and 90 mol/m^3 sodium chloride is $k_2 = 0.67313$ m^3/mol · s. As in the experiments, t_r (ms) was chosen to be 317, 181, 61, 28, 16.7, 9.5, 6.5, and 4.8. Therefore, the value of C_{A0} corresponding to $t_r = 317$ ms is 4.686 mol/m^3 and, thus, $A_0 = 9.373$ mol/m^3. The inlet concentration of B is $B_0 = 9.842$ mol/m^3 and $D_0 = 9.373$ mol/m^3 to satisfy the molar ratio of reagents (1:1.05:1) adopted in all the experimental runs. The inlet concentrations corresponding to the characteristic reaction times are summarized in Table 1.

As done in the experiments, the inlet jet Reynolds number, defined by

$$Re_j = \frac{d_1U_1}{\nu_1}, \tag{42}$$

is computed, based on the inlet velocity, the diameter of the inlet tube ($d_1 = 0.5$ mm), and the properties of the mixed stream as if only the first reaction has occurred. Note that Re_j represents the integral-scale Reynolds number in the CIJR. Thus, the local turbulence Reynolds number will scale like[6] $Re_1 \sim Re_j^{1/2}$. Hence, the micromixing time t_{SSS} will depend on Re_j through both the Re_j -dependence of C_ϕ, and the dependence of γ (Eq. 38) on $k/\varepsilon \sim Re_j^{-1}$. The overall dependence of the micromixing time on Re_j will, thus, scale like $t_{SSS} \sim [Re_jC_\phi(Re_j)]^{-1}$, and will vary from $t_{SSS} \sim Re_j^{-3/2}$ at low to moderate jet Reynolds numbers to $t_{SSS} \sim Re_j^{-1}$ at (very) high-jet Reynolds numbers. The jet Reynolds numbers and the corresponding inlet velocities adopted in the simulations are shown in Table 2 The standard $k - \varepsilon$ model in Fluent 6.2 with enhanced wall treatment, was employed to compute the turbulent kinetic energy and dissipation. Fluent 6.2 offers another two-wall treatment options: the standard wall functions and the nonequilibrium wall functions. However, they were not employed in our simulations since the law of the wall assumption is questionable for the three-dimensional (3-D) flow in the CIJR. The enhanced wall treatment involves a two-layer $k - \varepsilon$ model the performance of which is satisfactory for complex flows. More details can be found elsewhere.[16]

It should be noted that the length-to-diameter ratio, L/d, of the inlet feed tubes in the experiments was designed to be a minimum of eight to ensure that the jets were stable. However, in order to improve the computational efficiency, $L/d = 1.62$ in the computations. The inlet boundary conditions for the two jets are assumed to be identical and given by the outflow of a tube with $L/d = 10$. Similarly, in the experiments the exit-tube runner was designed to be at least 10 times the outlet diameter in order to ensure that the streams were fully mixed prior to sample collection. However, we use $K/\delta = 1.62$ in our com-

Table 2. Inlet Jet Velocity for Various Jet Reynolds Numbers

Re_j	100	200	400	500	600	800	1000	2000	3000	4000
U_1 (m/s)	0.415	0.83	1.66	2.10	2.49	3.32	4.15	8.30	12.45	16.6

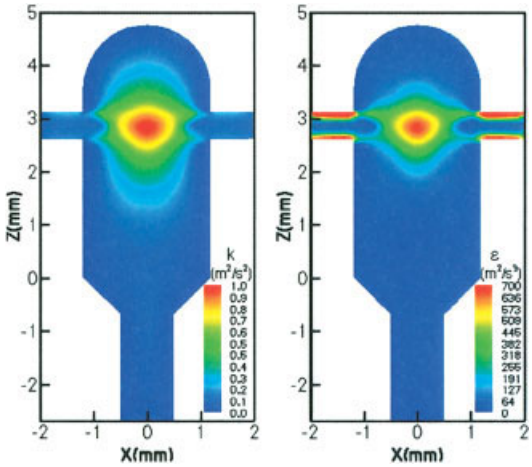

Figure 6. Turbulence fields for $Re_j = 400$.

[Color figure can be viewed in the online issue, which is available at www.interscience.wiley.com.]

putations. The simulation results revealed that unless t_r is small (for example, 4.8 ms), and the jet Reynolds number is not high enough (that is, $Re_j < 500$), the simulated conversion of D for a domain with $K/\delta = 10$ (Domain B) is very close to that for a domain with $K/\delta = 1.62$ (Domain A). More details are given in the discussion of the results later. Unless specified otherwise, the computational results are found using Domain A.

Because the density and viscosity are constant (that is, independent of the scalar fields), the turbulent flow field can be obtained first before solving the other scalar transport equations. Thus, for a fixed jet Reynolds number, the CFD solution procedure can be divided into three sequential steps:

1. Solve the turbulence model for $\langle \mathbf{U} \rangle$, k and ε.
2. Solve the nonreacting DQMOM-IEM model to find p_1, ξ_1 and ξ_2.
3. For each value of t_r, solve the reacting DQMOM-IEM model for Y_{21} and Y_{22}.

This procedure is facilitated by the ability to solve only selected transport equations in Fluent 6.2 while holding all other variables constant.

Results and Discussion

Turbulent-flow fields

Sample distributions of the turbulent kinetic energy and dissipation rate with $Re_j = 400$ are shown in Figure 6. The turbulent kinetic energy has a peak value at the interface of the impinging jets as expected. In general, the zone of intense mixing is limited to a small region of the total volume of the CIJR. At lower values of Re_j, fluid from the inlets can easily bypass the mixing zone and large-scale segregation is observed in the reactor and at the reactor outlet. The pressure drop across the CIJR is shown in Table 3 as a function of the jet Reynolds number. Note the substantial increase in the pressure drop between $Re_j = 1{,}000$ and 2,000. This increase is due to the formation of a turbulent zone at the reactor outlet as discussed later.

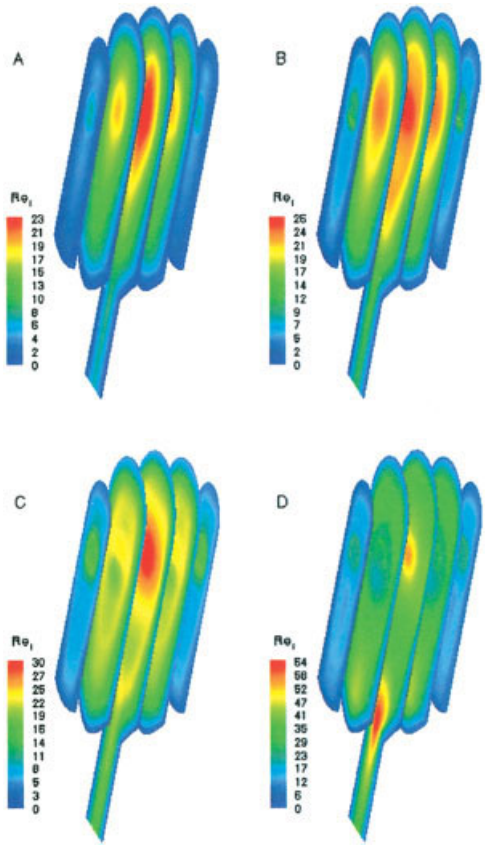

Figure 7. Turbulent Reynolds number in the CIJR for different values of Re_j. A: 200. B: 400. C: 1,000. D: 4,000.

[Color figure can be viewed in the online issue, which is available at www.interscience.wiley.com.]

Note that Re_1 is the ratio of the turbulence integral time scale $\tau_u = k/\varepsilon$ and the Kolmogorov timescale $\tau_\eta = (\nu/\varepsilon)^{1/2}$. Thus, at least conceptually, $Re_1 = 1$ would correspond to a flow with only one time scale (that is, laminar), and Re_1 increases proportional to the Taylor-scale Reynolds number[6] as the flow becomes more turbulent. Generally speaking, a flow must have $Re_1 \gg 10$ in order to be considered turbulent (that is, amenable to Reynolds-average turbulence models). Moreover, using the model energy spectrum,[11] it is possible to show[6] that $Re_1 > 100$ is required for the existence of an inertial range (that is, high-Reynolds-number flow). In general, care must be taken when using standard turbulence models for flows with $Re_1 < 10$.

Re_1 in the CIJR varies with Re_j as shown in Figure 7. When $Re_j = 200$, $Re_1 < 23$ everywhere except in a small central core of the impingement zone, indicating that the predictions of the turbulence model must be treated with caution when $Re_j \leq 200$. When, $Re_j = 400$, $Re_1 \leq 26$ in much of the flow, indicating that

Table 3. Pressure Drop Across CIJR for Various Jet Reynolds Numbers

Re_j	100	200	400	500	600	800	1000	2000	3000	4000
Δp (psia)	214.1	565.2	1528	2186	2843	4552	6680	23720	38910	45460

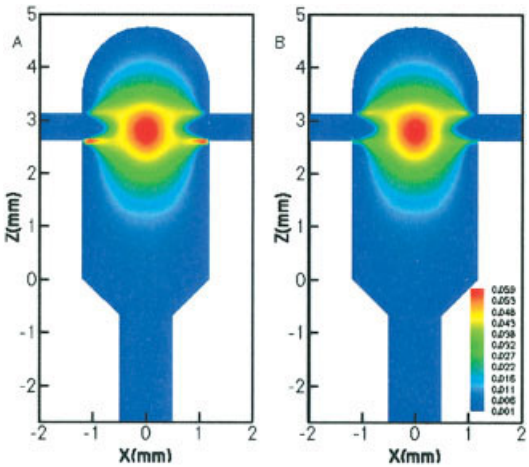

Figure 8. Contours of mixture-fraction variance $\langle \xi'^2 \rangle$ on the central plane for $Re_j = 400$ predicted by (A) the DQMOM-IEM model, and (B) the Reynolds-average transport equation.

[Color figure can be viewed in the online issue, which is available at www.interscience.wiley.com.]

the flow is moderately turbulent (although no inertial range exists). When $Re_j = 1{,}000$, $Re_1 \leq 30$ in much of the flow. Hence, as noted earlier, the flow in a CIJR cannot be considered to be fully developed turbulence in most of the range considered in the experiments. When $Re_j = 4{,}000$, a second zone of turbulence with $Re_1 \leq 64$ is found at the outlet to the reactor. It is this zone that changes the scaling behavior of the mixing times for $Re_j > 1{,}000$, seen later. Due to the high anisotropy of the flows in the CIJR, the turbulent field and the mixing timescales predicted tend to be affected by the turbulence model. As done elsewhere,[17,18] it would be useful to validate the turbulence-model predictions against microscale particle-image velocimetry (micro-PIV) measurements of $\langle \mathbf{U} \rangle$ and k in the CIJR or conventional PIV measurements in a suitably scaled CIJR.

Mixture-fraction fields

Figure 8 shows contour plots of the mixture-fraction variance predicted by the DQMOM-IEM model, and by the Reynolds-average transport equation at the central plane of the CIJR with $Re_j = 400$. The mixture-fraction mean and variance at different Z-positions are shown in Figure 9. The results given by the DQMOM-IEM model are very close to those given by the Reynolds-average transport equations, indicating that the DQMOM-IEM model predicts the first-order and second-order moments of the mixture fraction consistently. As done elsewhere,[18] it would be useful to validate these predictions using planar laser-induced fluorescence (PLIF) measurements in a CIJR.

If the dissipation term, ε_ϕ, is set to zero (this is equivalent to turning off the micromixing terms in the DQMOM-IEM simulations), the mixture-fraction variance is related to the mixture-fraction mean analytically by[18]

$$\langle \xi'^2 \rangle = \langle \xi \rangle (1 - \langle \xi \rangle) \tag{43}$$

Figure 10 shows that the RANS and DQMOM-IEM simulations agree with Eq. 43. We should note, however, that in order to obtain good agreement for the RANS simulation a significantly finer grid is required than for the DQMOM-IEM simulations. This difference is due to the structure of the models (that is, when $\varepsilon_\phi = 0$, the mixture-fraction variables ξ_n are constant in the DQMOM-IEM model and only the values of p_n change), and in general the solution to the DQMOM-IEM model will be less sensitive to the grid refinement. Thus, when the RANS model is employed, the case with $\varepsilon_\phi = 0$ can be used to check for grid independence via Eq. 43. Analogous remarks hold for the LES model of the SGS mixture-fraction variance.

The volume-averaged LSS and SSS time scales in the CIJR decrease with increasing Re_j as shown in Figure 11. Consistent with the dependence of the residence time in the CIJR on Re_j, t_{LSS} scales like Re_j^{-1}. In contrast, t_{SSS} falls off at a faster rate, but with a slope that depends on Re_j. As anticipated in our discussion of the scaling of Re_1 with Re_j, the observed slope is due to the fact that C_ϕ increases with Re_1 (and, hence, with

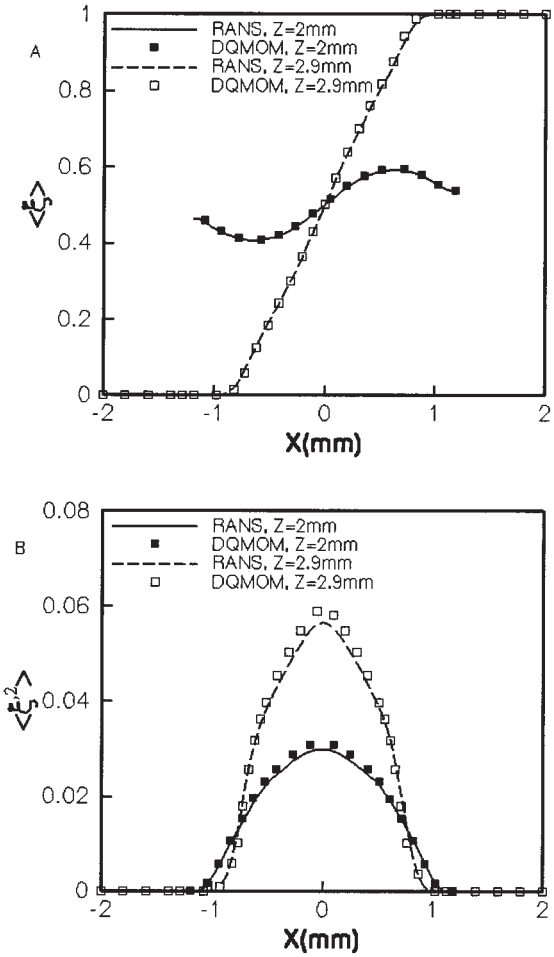

Figure 9. Profiles on the central plane of mixture-fraction mean (A) and variance (B) for $Re_j = 400$ predicted by the DQMOM-IEM model, and the Reynolds-average transport equations at different Z-positions.

(See Figure 8 for location of Z.)

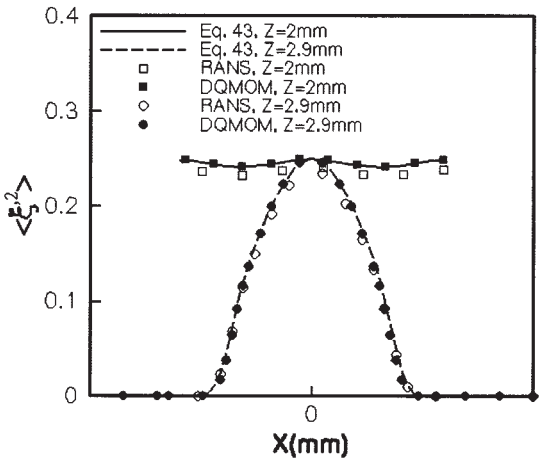

Figure 10. Profiles on the central plane of mixture-fraction variance for $Re_j = 400$ predicted by the DQMOM-IEM model, and the Reynolds-average transport equations with no dissipation at different *Z*-positions. (See Figure 8 for location of *Z*.)

Re_j). It can be seen that in the range of jet Reynolds numbers from 500 to 1,000, the micromixing time scales approximately like $Re_j^{-3/2}$ due to the Reynolds-number dependence of C_ϕ. Nevertheless, at jet Reynolds numbers greater than 1,000, C_ϕ approaches its high-Reynolds-number limiting value shown in Figure 5, in which case the micromixing time scales like Re_j^{-1}. In the literature, this change of slope has been referred to as a transition from "micromixing" to "mesomixing".[15] Here we interpret it instead as a *low-Reynolds-number effect* where for $Re_j < 1{,}000$ scalar spectrum has *no inertial-convective subrange*. Thus, if the change of shape of the scalar spectrum is appropriately accounted for, we argue that the distinction between "micromixing" and "mesomixing" is unnecessary for this flow. Instead, they can both be related to the scalar dissipation rate (which is the accepted measure of molecular mixing in the turbulent-mixing community[11,6]) using the integral method proposed by Corrsin.[13]

Finally, note that due to the Re_1-dependence of C_ϕ there exists a crossover point in Figure 11 near $Re_j \approx 400$ marking a change from SSS-controlled mixing at low-Reynolds numbers to LSS-controlled mixing at high-Reynolds numbers. The effect of this crossover is also observable in the DMP conversion results shown later. On the basis of the turbulence theory,[11] there is no fundamental reason to expect that t_{SSS} should ever be larger than t_{LSS}. Thus, the existence of a crossover point can be interpreted as an indication that a low-Reynolds-number (or Schmidt-number) correction is also needed for the turbulent Schmidt number Sc_T appearing in Eq. 17 (which determines Γ_T and, hence, t_{LSS}). From a chemical-reaction-engineering perspective, operating at low-jet-Reynolds numbers should be avoided due to the relatively poor mixing conditions. Nevertheless, from a CFD-modeling perspective it would most likely be possible to improve the predictions for low jet Reynolds numbers by resorting to large-eddy simulations (LES), which resolve the large-scale eddies in the flow. We, thus, note in passing that with suitable modifications to the parameters,[6] the DQMOM-IEM model can be applied to model reactive mixing in the context of LES, and, thus, could easily be implemented with the LES models available in Fluent 6.2.

Concentration fields

Representative distributions of the Reynolds-average species (H^+, OH^- and DMP) are shown in Figure 12. When $Re_j = 400$ and $t_r = 61$ ms, H^+ is consumed completely and little OH^- is left in the outflow. The concentration of DMP does not change much outside of the reaction zone (defined quantitatively later). For the CIJR experiments, no information about the local concentration distributions is available. Thus, it would be useful to validate these CFD predictions using local planar laser-induced fluorescence (PLIF) measurements of an acid-base reaction with a pH-sensitive dye.[19]

DMP conversion

The conversion of DMP (Eq. 28) is shown in Figure 13 for both the experiments[1] and the CFD simulations as a function of the jet Reynolds number (Re_j) and the characteristic reaction time (t_r). When $400 \leq Re_j$ and $t_r \geq 9.5$ ms, the simulation results and the experimental measurements are in close agreement. The conversion decreases when Re_j increases, indicating (as expected) that poor mixing favors the slow reaction. Once $Re_j \geq 2000$, X changes more slowly with Re_j due to the creation of the turbulent zone at the outlet to the CIJR seen in Figure 7.

For $t_r < 9.5$ ms, the experimental curves show higher conversion (that is, poorer mixing) than the simulations. Because the agreement for larger t_r is good, and the species do not affect the flow field, this anomaly cannot be assigned to a change in the micromixing time. In order to test if the CFD code was generating an anomalous upper limit, we set $t_r = 0$, and computed the dashed line at $X = 0.85$ appearing in Figure 13. Although this is slightly lower than the theoretical limit X_{max}, it is well above the experimental curve for $t_r = 4.8$ ms. Thus, the poor agreement cannot be assigned to the numerics used in the CFD code. In their analysis of the data, Johnson and Prud'homme[1] show that for $t_r \leq 6.5$ ms, the data do not follow the expected experimental scaling law. We are, thus, inclined to believe that other factors (such as incomplete reaction in the

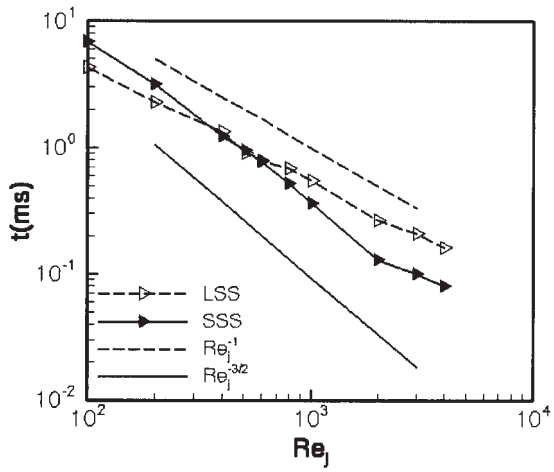

Figure 11. Dependence of volume-averaged time scales on Re_j.

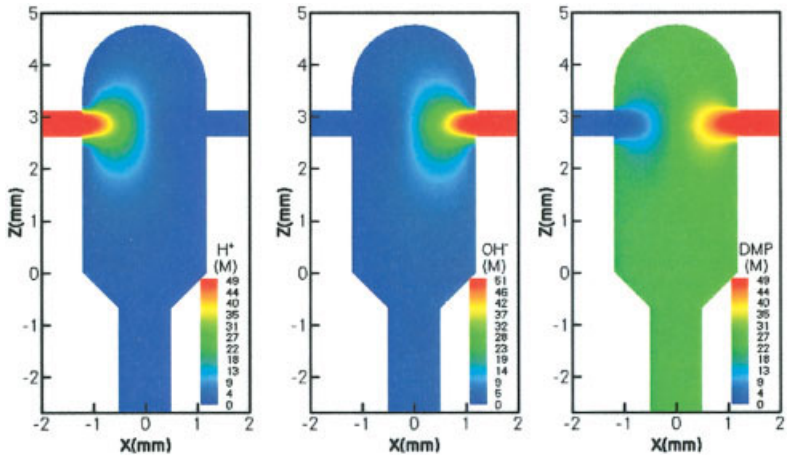

Figure 12. Reynolds-average species distributions for $Re_j = 400$ and $t_r = 61$ ms.

[Color figure can be viewed in the online issue, which is available at www.interscience.wiley.com.]

CIJR as discussed later) are involved that cannot be captured in the CFD model.

When $Re_j = 100$ and $t_r = 317$ ms, the computed conversion is much lower than the experimental value. This is due to the fact that for $Re_j < 200$, the flow has a turbulence Reynolds number that is too low for the turbulence model to work correctly. Indeed, as discussed earlier, the accuracy of the micromixing parameter C_ϕ, and the turbulent diffusivity Γ_T predicted by the standard $k - \varepsilon$ model at low jet Reynolds numbers are questionable. Nevertheless, the combined $k - \varepsilon$, DQMOM-IEM model works satisfactorily when the flow is more turbulent (that is, $200 \leq Re_j$).

By adding a polymer, the molecular viscosity of the inlet streams was increased in the experiments to 0.0071 kg/m · s. The conversion of DMP as a function of Re_j is shown in Figure 14. Note that most of the experimental data are in the low to very-low range of turbulence Reynolds numbers where (as discussed earlier) we cannot expect good agreement. On the other hand, for $Re_j \geq 200$ the agreement is satisfactory. We should stress, however, that for these data the Reynolds number is so low that *no inertial-convective subrange exists*. For this reason, one cannot except to find for large Schmidt numbers anything but viscous-convective scaling for the micromixing time scale. Moreover, because the range of length scales in the velocity field is very narrow, such low-Reynolds-number flows have more in common with chaotic mixing[20] than with high-Reynolds-number turbulent mixing. In any case, if such low-Reynolds-number flows in a CIJR were of technological interest, they could be computed directly using direct-number simulation for the velocity field[11] and a subgrid-scale mixing model (like DQMOM-IEM) for the scalar field.

Effect of outflow boundary location

The outlet conversions found when $Re_j = 400$ and $t_r = 4.8$ ms using Domains A and B are 0.362 and 0.364, respectively. The values for other Reynolds numbers are given in Table 4. The differences between values at the same Reynolds number are small and might lead one to assume that the outlet stream is well mixed. However, this is not always the case. The effect of K/δ on the outflow concentration distributions when $Re_j = 400$ and $t_r = 4.8$ ms is shown in Figure 15. From this figure, it

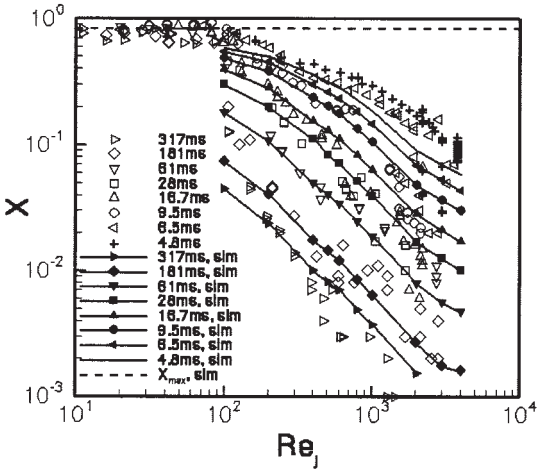

Figure 13. Conversion of DMP vs. Re_j in the CIJR.

Open symbols: experiments. Closed symbols: simulations.

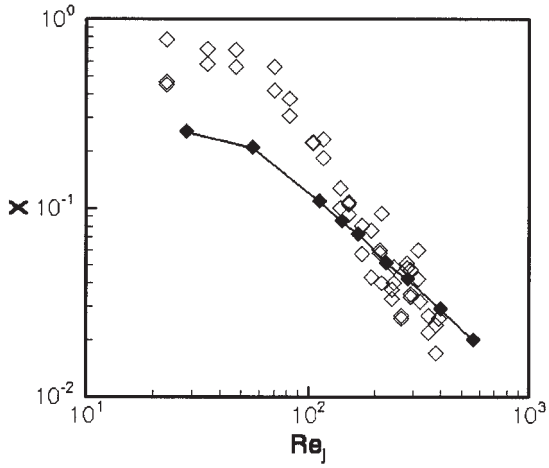

Figure 14. Effect of increased molecular viscosity on DMP conversion for $t_r = 29.7$ ms.

Table 4. Effect of Outflow Boundary Location on Conversion for t_r = 4.8 ms

Re_j	100	200	400	500	600	800	1000
X (Domain A)	0.588	0.505	0.362	0.320	0.286	0.230	0.185
X (Domain B)	0.592	0.505	0.364	0.322	0.286	0.233	0.188

can clearly be seen that the mixture fractions in the two environments are not uniform across the outflow boundary, indicating that the outlet streams are not completely mixed in the CIJR when the Reynolds number and mixing rates are too low. The reactions will, thus, continue (under poorly mixed conditions!) after the outlet, and the conversion of DMP will change before the collection point used in the experiments (that is, the end of the outlet tube). This may be one reason why the measured conversions are higher than the computed values for $t_r < 9.5$ ms in Figure 13. The effect of K/δ becomes weaker as Re_j increases due to creation of the turbulent zone at the outlet of the CIJR (Figure 7), or as t_r decreases, under which conditions the reactions have less effect on the conversion. In order to determine when the reaction zone extends into the outlet of the CIJR, we have developed a method to visualize the reaction and segregation zones described next.

Reaction and segregation zones

In the scaling theory developed by Johnson and Prud'homme,[1] the zones in the CIJR where energy is dissipated or "mesomixing" and reactions occur are required to complete the scaling law. As noted by these authors, one of the advantages of CFD is that such zones can easily be visualized and studied, for example, as a function of the jet Reynolds number. Of particular interest are the reaction zone (defined later), and the zones with significant large-scale and small-scale segregation.

From Eq. 13, it can be seen that the second reaction only occurs at spatial locations where

$$0 \le \xi_1(\mathbf{x}, t) \le \xi_{s1} \quad \text{or} \quad 0 \le \xi_2(\mathbf{x}, t) \le \xi_{s1}$$

We will refer to such regions in the CIJR as the reaction zone (RZ). Note that this definition of the reaction zone includes regions where the second reaction is very slow (that is, $\xi \approx \xi_{s1}$), and, hence, essentially negligible. In order to have a more precise definition of the reaction zone, we can define a *local* mixing time by

$$t_{\text{mix}} = t_{\text{LSS}} + t_{\text{SSS}} \tag{44}$$

and a *local* Damköhler number using Eq. 13

$$Da_{\text{loc}}(\xi) = t_{\text{mix}} A_0 k_2 \left(1 - \frac{\xi}{\xi_{s1}}\right) \quad \text{for } 0 \le \xi \le \xi_{s1} \tag{45}$$

and zero otherwise. Note from Figure 11 that the volume-averaged local mixing time decreases from approximately 10 ms at Re_j = 100 to approximately 0.3 ms at Re_j = 2,000.

The local Damköhler number found from Eq. 45 is shown for Re_j = 400 and 1,000 with t_r = 4.8 ms in Figure 16. Because $\xi_1 \le \xi_2$, only the Damköhler number in environment 1 is shown. From this figure, we can observe that $Da_{\text{loc}} \le 1$, indicating that the mixing is relatively good at these Reynolds numbers. Moreover, as expected, the Damköhler number decreases with increasing Reynolds number. We can also observe that the bulk of the conversion occurs on the side of the CIJR where the acid enters the reactor, and that this zone extends along the entire height of the CIJR. Thus, relative to the reaction time scales, macromixing is not particularly good in this reactor, and bulk-scale segregation cannot be neglected when modeling the CIJR.

In the reaction zone, the reactions are controlled by large-scale segregation (LSS) alone if

$$\langle \xi'^2 \rangle_{\text{LSS}} \ge \sigma^2 \quad \text{and} \quad \langle \xi'^2 \rangle < \sigma^2,$$

where we define the cut-off standard deviation σ to be the distance in mixture-fraction space (see Figure 2) from the end of reactions (ξ_{s1}) to complete mixing ($\bar{\xi}$)

$$\sigma = \bar{\xi} - \xi_{s1} = 0.0122.$$

Note that the exact choice of σ is not crucial: it just serves as a cut-off point for defining regions in the flow field. An

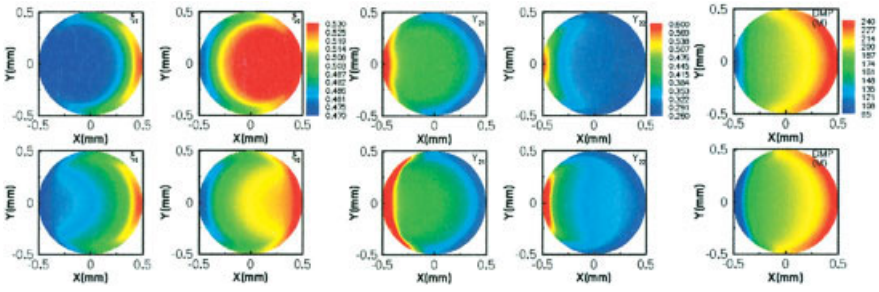

Figure 15. Distribution of the mixture fraction, reaction-progress variable, and DMP on the outflow surface for Re_j = 400 and t_r = 4.8 ms.

Top row: Domain A (K/δ = 1.62). Bottom row: Domain B (K/δ = 10). [Color figure can be viewed in the online issue, which is available at www.interscience.wiley.com.]

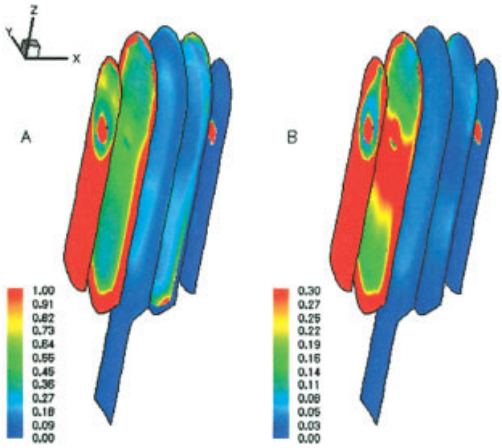

Figure 16. Profiles of the local Damköhler number in environment 1 for t_r = 4.8 ms. A: Re_j = 400. B: Re_j = 1,000.

[Color figure can be viewed in the online issue, which is available at www.interscience.wiley.com.]

alternative representation of the LSS and SSS zones could be found by using contour plots like the ones shown in Figure 8.

In the reaction zone, the reactions are controlled by small-scale segregation (SSS) alone if

$$\langle \xi'^2 \rangle_{\mathrm{LSS}} < \sigma^2 \quad \text{and} \quad \langle \xi'^2 \rangle \geq \sigma^2,$$

or by both LSS and SSS if

$$\langle \xi'^2 \rangle_{\mathrm{LSS}} \geq \sigma^2 \quad \text{and} \quad \langle \xi'^2 \rangle \geq \sigma^2.$$

The distributions of the various reaction and mixing zones for Re_j = 400 and Re_j = 1,000 are shown in Figure 17.

From this figure, we can observe that the volume of the reaction zone decreases slightly when Re_j increases, indicating that the overall mixing process is faster. Nevertheless, the reaction zone extends into the outlet tube since macromixing is not complete (see Figure 12). On the axis of the inlet jets, the reactions are controlled by both LSS and SSS. In contrast, the region where the reactions are controlled only by SSS has the form of a distorted torus around this axis. Note that the SSS-controlled region shrinks with increasing Re_j due to the increase in C_ϕ. Also note that there is no region where reactions are controlled by LSS alone.

From the reaction zone in Figure 17 and from Figure 15, we can observe that complete mixing at all scales is not achieved in the CIJR (that is, ξ_1 is not larger than ξ_{s1} at all points on the outlet surface). We can, therefore, conclude that although the CIJR enables intense micromixing, the flow does not macromix completely during its residence time in the reactor. In order to avoid that the reaction zone extends beyond the CIJR, it would suffice to separate more $\bar{\xi}$ from ξ_{s1}. If equal flow rates are used (thereby keeping the flow field unchanged and $\bar{\xi}$ constant), this can be done by making ξ_{s1} smaller (for example by increasing B_0 or decreasing A_0). From the plots of ξ_1 in Figure 15, we can observe that lowering ξ_{s1} to 0.470 would be sufficient to avoid reactions in the outflow for $Re_j \geq 400$. Another alternative would be to make the outlet tube diameter smaller in order to decrease LSS at the outflow. This method has been investigated experimentally.[1] A disadvantage of employing this method would be an increase in the pressure drop across the CIJR.

Conclusions

The major conclusion that can be drawn from this work is that a CFD model based on fundamental turbulent-transport theory can accurately predict the experimental conversion data[1] in the range of jet Reynolds numbers corresponding to turbulent flow. We have also demonstrated that the method[13] for determining the micromixing time as a function of turbulent Reynolds number and Schmidt number can be combined with the model scalar spectrum[6] to accurately account for the Reynolds- and Schmidt-number effects present at low-jet Reynolds numbers. Thus, when combined with accurate chemical-rate expressions, the CFD model used in this work should be adequate for design and scaleup of CIJRs for other processes.

The secondary conclusions pertain to the particular CIJR used in the CFD simulations. These conclusions are as follows:

1. Although the mixing times are short, the turbulent flow in the CIJR is not fully developed for the jet Reynolds numbers used in the experiments. It is, thus, crucial to account for Reynolds- and Schmidt-number effects on the micromixing time scale.

2. Low-Reynolds-number effects are responsible for the experimentally observed Kolmogorov scaling of the micromixing time. At higher jet Reynolds numbers, inertial-range scaling is observed in accordance with turbulent-mixing theory.

3. Despite rapid mixing, the outlet stream is not completely mixed. Thus, because the reactant concentrations (that is, ξ_{s1}.) were chosen such that conversion continues to increase nearly up to the point of complete mixing, the reaction zone extends into the outlet tube. As pointed out in the discussion, this can be avoided in future experimental studies by lowering ξ_{s1}.

Finally, because the experimental data were limited to overall conversion, it was not possible to validate the *local* turbulence and concentration fields predicted by the CFD model. We would thus recommend that future experimental studies of the CIJR include PIV and PLIF measurements of the local velocity and scalar fields. As shown elsewhere[18] for a confined planar-

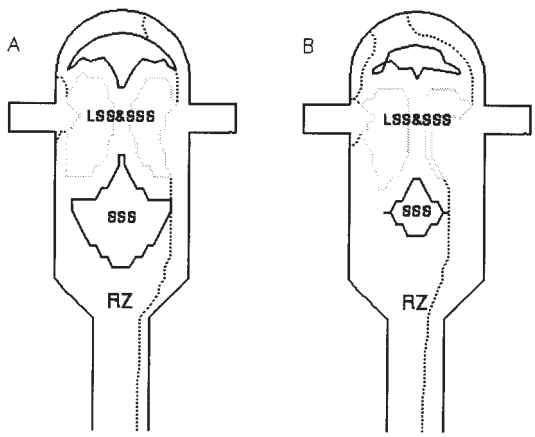

Figure 17. Distribution of the reaction (RZ) and segregation (LSS, SSS) zones for (A) Re_j = 400 and (B) Re_j = 1,000.

jet reactor, these data would be extremely valuable for validating the turbulence and scalar-mixing models used in the CFD simulations.

Acknowledgments

This work has been made possible by grants (CTS-0336435 and CTS-0403864) from the U. S. National Science Foundation.

Literature Cited

1. Johnson BK, Prud'homme RK. Chemical processing and micromixing in confined impinging jets. *AIChE J*. 2003;49:2264-2282.
2. Mahajan AJ, Kirwan DJ. Rapid precipitation of biochemicals. *J of Phys D - Appl Phys*. 1993;26:B176–B180.
3. Mahajan AJ, Kirwan DJ. Micromixing effects in a two-impinging-jets precipitator. *AIChE J*. 1996;42:1801-1814.
4. Johnson BK, Prud'homme RK. Flash nanoprecipitation of organic actives and block copolymers using a confined impinging jets mixer. *Australian J of Chem*. 2003;56:1021-1024.
5. Johnson BK, Prud'homme RK. Mechanism for rapid self-assembly of block copolymer nanoparticles. *Phys Rev Lett*. 2003;91.
6. Fox RO. Computational models for turbulent reacting flows. Cambridge: Cambridge University Press; 2003.
7. Marchisio DL, Fox RO. Solution of population balance equations using the direct quadrature method of moments. *J of Aerosol Sci*. 2005;36:43-73.
8. Villermaux J, Devillon JC. Représentation de la coalescence et de la redispersion des domaines de ségrégation dans un fluide par un modèle d'interaction phénoménologique. Proceedings of the 2nd *International Symposium on Chemical Reaction Engineering*, New York; Elsevier; 1972:1-13.
9. Wang L, Fox RO. Comparison of micromixing models for CFD simulation of nanoparticle formation. AIChE Journal. 2004;50:2217-2232.
10. Baldyga J, Bourne JR, Walker B. Nonisothermal micromixing in turbulent liquids: theory and experiment. *Canadian J of Chem Eng*. 1998;76:641-649.
11. Pope SB. Turbulent flows. Cambridge: Cambridge University Press; 2000.
12. Bird RB, Stewert WE, Lightfoot EN. Transport phenomena. New York: John Wiley & Sons, Inc; 2002.
13. Corrsin S. The isotropic turbulent mixer: part II. arbitrary Schmidt number. *AIChE J*. 1964;10:870-877.
14. Baldyga J, Bourne JR. A fluid mechanical approach to turbulent mixing and chemical reaction - Part II Micromixing in the light of turbulence theory. *Chem Eng Communications*. 1984;28:243-258.
15. Baldyga J, Bourne JR. Turbulent mixing and chemical reactions. New York: Wiley; 1999.
16. Chen HC, Patel VC. Near-wall turbulence models for complex flows including separation. *AIAA J*. 1988;26:641-648.
17. Li H, Ewoldt R, Olsen MG. Turbulent and transitional velocity measurements in a rectangular microchannel using microscopic particle image velocimetry. *Experimental Thermal and Fluid Sci.* 2005; 29: 435-446.
18. Feng H, Liu Y, Olsen MG, Fox RO, Hill JC. Investigation of turbulent mixing in a confined planar-jet reactor. *AIChE J*. 2005;51:2649–2664.
19. Koochesfahami MM, Dimotakis PE. Mixing and chemical reactions in a turbulent liquid mixing layer. *J of Fluid Mechanics*. 1986;70:83-112.
20. Ottino JM. The kinematics of mixing: stretching, chaos, and transport. Cambridge: Cambridge University Press; 1989.

Manuscript received Jan. 27, 2005, and revision received Jun. 15, 2005.